RSC Advances

PAPER

View Article Online
View Journal | View Issue

Cite this: *RSC Adv.*, 2025, **15**, 21687

Microemulsion synthesis and optical temperature sensor properties in HA/β-TCP composite phosphors

Cao Xuan Thang,[a] Duy-Hung Nguyen,[a] Vuong-Hung Pham,[a] Nguyen Viet Tung,[a] Do Danh Bich[b] and Hoang Nhu Van *[c]

Herein, a novel microemulsion (ME) method for the synthesis of rare earth-element-doped hydroxyapatite (HA)/beta-tricalcium phosphate (β-TCP) composite phosphors was performed and yielded phosphors with intense green upconversion (UC) emission and high temperature sensitivity. The effect of polyvinyl alcohol (PVA) content on the structure and luminescence properties of the phosphors was investigated in detail. X-ray diffraction and Raman spectra showed that the mixed phases included the main hexagonal HA phase and the secondary orthorhombic β-TCP phase. Under 975 nm excitation, the obtained phosphors exhibited strong green UC emission, and their intensity depended on PVA content. Notably, the fluorescence intensity ratio technique revealed that the phosphors had a high color purity of up to 94.77% and high temperature sensitivity of 0.93% K^{-1} at 293 K. These results indicate that the phosphors are suitable for applications in thermal sensors and optoelectronic devices.

Received 9th April 2025
Accepted 30th May 2025

DOI: 10.1039/d5ra02458g

rsc.li/rsc-advances

1. Introduction

Measuring temperature accurately is important because it is a key physical parameter in science and daily life.[1–3] In conventional contact temperature measurement, liquid-filled glass thermometers and thermocouples are used to determine temperature. However, these devices present numerous limitations, including low sensitivity, limited response times, and the inability to measure under harsh conditions,[4–6] hindering the above method. Noncontact temperature measurement methods based on rare earth (RE) ion-doped phosphor materials (*via* optical temperature sensors) are widely used to overcome the above-mentioned limitations. RE ion-doped upconversion (UC) materials possess excellent luminescence properties[4,6] and have two energy levels that act as two thermocouples with energy from 200 cm^{-1} to 2000 cm^{-1} making them suitable for thermal sensors.[4,7] Among other methods, the fluorescence intensity ratio (FIR) technique is selected to explore materials for optical thermal sensors[8–10] based on observations of the emission intensity changes of two energy levels (RE^{3+} ion) on temperature.[11,12] The advantages of this method are independent activators, spectrum losses, and fluctuations in excitation intensity, suggesting good measurement accuracy and high resolution and reliability.[13,14] The Er^{3+} ion has two levels ($^2H_{11/2}$ and $^4S_{3/2}$) with different energies approximately 800 cm^{-1},[13] suggesting that it is suitable as an activator for temperature sensor based phosphors. Recently, researchers have achieved good thermal sensing properties on the basis of the selective enhancement of the green UC emission of phosphors.[1,15–17] In particular, our previous work realized the intense green UC emission with good optical thermal sensing based on RE ion-doped phosphors.[8,18–20] Therefore, good optical thermal sensing properties based on biocompatible RE-doped HA could extend applications in the optoelectronic and biomedical fields.

Hydroxyapatite, $Ca_6(PO_4)_{10}(OH)_2$, (HA) is an attractive material that is widely utilized in biomedical applications, including bone cement and replacement material, drug delivery platforms, and bioimaging methods, because of its excellent bioactivity, biocompatibility, high osteoconductivity, and similarity to the inorganic components of bone and teeth in mammals.[21–24] The flexible structure of HA enables the substitution of various ions at the Ca^{2+}, PO_4^{3-}, and OH^- sites of its host.[25,26] Many approaches for the successful synthesis of RE–doped HA have been used to acquire good mechanical performance, as well as excellent physicochemical properties. They include microwave irradiation,[27] coprecipitation,[28] the hydrothermal method,[8] and microemulsion (ME) method.[29] The ME method could serve as a good choice for synthesizing materials with high crystallinity, controlled morphology, and narrow-size distribution.[30,31] Moreover, this approach presents several advantages, such as high thermodynamic stability; easy nanoparticle synthesis; and particle dispersion reaggregation, which could achieve spherical shapes in nanodimensions.[31,32] The structure of ME systems includes three phases: water, oil, and

[a]*School of Materials Science and Engineering (SMSE), Hanoi University of Science and Technology (HUST), Hanoi, Vietnam*

[b]*Faculty of Physics, Hanoi National University of Education, Cau Giay, Hanoi, Vietnam*

[c]*Faculty of Materials Science and Engineering, Phenikaa University, Yen Nghia, Ha-Dong District, Hanoi 12116, Vietnam. E-mail: van.hoangnhu@phenikaa-uni.edu.vn*

a surfactant (cosurfactant) phase.[33] Cyclohexane and hexane are used as oil phases; cetyltrimethylammonium bromide (CTAB) and dimethyl sulfoxide (DMSO) have been applied as surfactants, wheseas the alcohols, such as *n*-butanol, *n*-pentanol, and polyvinyl alcohol (PVA), are employed as cosurfactants.[31–33] The oil-to-surfactant, cosurfactant-to-surfactant, and water-to-surfactant molar ratios strongly affect the morphology and size distribution of the ME systems.[32,33] Notably, PVA is widely used in artificial bone formation and biomedical applications, including drug delivery devices, orthopedic devices, and artificial organs because of its excellent properties as a nonionic, biocompatible, nontoxic surfactant with a high elastic modulus and biodegradability in water.[34–36] Nano-HAP-PVA gel can be prepared through PVA-assisted HA synthesis and exhibits excellent mechanical properties and bioactivities. Furthermore, the combination of biopolymers with nanoparticle fillers to obtain new materials with enhanced mechanical and electronic properties has been investigated.[35–37] Previous works have indicated that in HA synthesis, PVA could control morphology to small sizes and decrease agglomeration, making it suitable for organs, such as teeth and bone, that are well-ordered by surfactants.[34,37] Zeng *et al.*[21] synthesized nano-HA for sustained transdermal delivery through the ME method. They found that the optimal ME formula had the composition (w/w) of 13% lecithin, 26% *n*-propanol, 53% IPM, and 8% water. Furthermore, this material showed enhanced drug loading efficiency, thereby demonstrating a long-term inflammatory cell suppression effect. Montoya *et al.*[30] investigated HA nanoparticles synthesized by using reverse ME to explore the adsorption/desorption properties of enrofloxacin. Their results revealed that HA nanoparticles could be loaded with 92% enrofloxacin in solution and deliver 74% of the antibiotic during the first 12 h. Meanwhile, Prakash *et al.*[34] successfully synthesized spherical HA nanoparticles (approximately 20 nm) by using PVA as a cosurfactant. They showed that which surfactants have a strong effect on HA synthesis because the use of PVA and DMSO as a growth regulator can result in fine nanometer-sized HA material. Moreover, they demonstrated that this method is a novel approach for synthesizing HA nanoparticles. However, the ME synthesis of RE^{3+}-doped HA with intense green UC emission and good optical thermal sensing properties using PVA as a cosurfactant to control morphology has not yet been documented.

Herein, we report the novel ME synthesis of rare-earth doped HA/β-TCP phosphor with intense green emission for optical thermal sensors. The effect of PVA as a cosurfactant on the structure, morphology, and green emission properties of the system was investigated. The optical thermal sensing characteristics of the phosphors were explored by using the FIR technique.

2. Experimental procedures

A series of HA/β-TCP: Er/Yb/Mo nanocomposite phosphors with different contents of the cosurfactant PVA was synthesized through ME. Raw materials with high purity were used to synthesize the phosphors. They included $Ca(NO_3)_2$ (Aldrich, 99.9%), $Yb(NO_3)_3$ (Merck, 99.99%), $NH_4H_2PO_4$ (Aldrich, 99.9%), $(NH_4)_6Mo_7O_{24}$ (Aldrich, 99.9%), $Er(NO_3)_3$ (Merck, 99.99%), ammonia solution (Aldrich, 99.9%), *n*-hexane (Aldrich, 99.9%), PVA (Aldrich, 99.9%), dimethyl sulfoxide (Aldrich, 99.9%), and deionized (DI) water. The contents of dopant ions, such as Er^{3+}, Yb^{3+}, and Mo^{6+}, were fixed at 2, 15, and 5 mol%, respectively, with reference to the Ca^{2+} content, whereas the Ca/P molar ratio was kept constant at 1.67. Aqueous solutions of Ca^{2+} (1 M), $H_2PO_4^-$ (0.6 M), Er^{3+} (0.1 M), Yb^{3+} (0.1 M), and Mo^{6+} (0.1 M) were prepared by dissolving salts in DI water under magnetic stirring. PVA (0.05 M) was procedured by dissolving it on DI water and stirring at 80 °C. The PVA volumes were 5, 10, 15, and 20 ml (the corresponding samples were labeled as S1, S2, S3, and S4), whereas the DMSO and *n*-hexane contents were fixed at 10 and 50 ml per sample, respectively. In this process, DMSO was used as a primary surfactant. The volum ratios of oil/water/surfactant and cosurfactant used in this work were 5 : 2 : 1.5, 5 : 2 : 2, 5 : 2 : 2.5, and 5 : 2 : 3. The surfactant (DMSO) and cosurfactant (PVA) were added to *n*-hexane and stirred for 30 min to obtain the oil

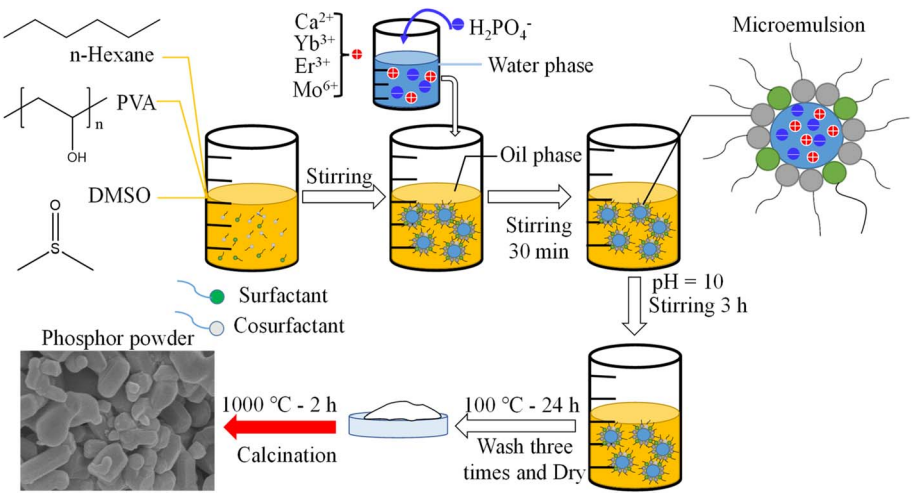

Fig. 1 The schematic synthesis of phosphors by microemulsion method.

phase. The water phase (20 ml) was obtained by adding the anion solution ($H_2PO_4^-$) dropwise to the cation solution (Ca^{2+}, Er^{3+}, Yb^{3+}, and Mo^{6+}) and stirring the resulting mixture for 45 min. Afterward, the water phase was added dropwise to the oil phase to form an ME system. The system was controlled at pH 10 by using NH_3 solution and continuously stirred for 3 h. Lastly, the precipitate was collected, washed three times with DI water and alcohol, then dried at 100 °C for 24 h. The obtained powder was annealed at 1000 °C for 2 h to prepare phosphor materials. The typical steps to synthesize the phosphor samples are depicted in Fig. 1.

The phosphor samples were analyzed by using an X-ray diffractometer (XRD, Bruker D8 Advance), field emission scanning electron microscope (FE-SEM, JEM 1010, JEOL Techniques, Tokyo, Japan), Fourier-transform infrared spectrometer (FT-IR, PerkinElmer spectrum BX), and Raman spectrometer (MacoRAM, Horiba) to determine crystal structure, morphology, and chemical bonding. The luminescence emission behaviors of all synthesized samples were determined by using a NANOLOG spectrophotometer (Horiba, USA) coupled with a 975 nm excitation laser source and heating controller. The X-ray photoelectron spectroscopy (XPS, VG Scientific, ESCALAB250). Thermal sensing properties were determined by using the FIR technique based on the dependence of emission intensity on temperatures ranging from 293 K to 533 K.

3. Results and discussion

3.1. Effect of PVA content on the structure of the phosphors

The structures of the samples synthesized through the ME technique with different PVA contents were characterized by using XRD measurements, as shown in Fig. 2. In accordance with the standard cards of HA (PDF# 01-079-5683) and β-TCP (PDF# 09-0169), all diffraction peaks matched their references

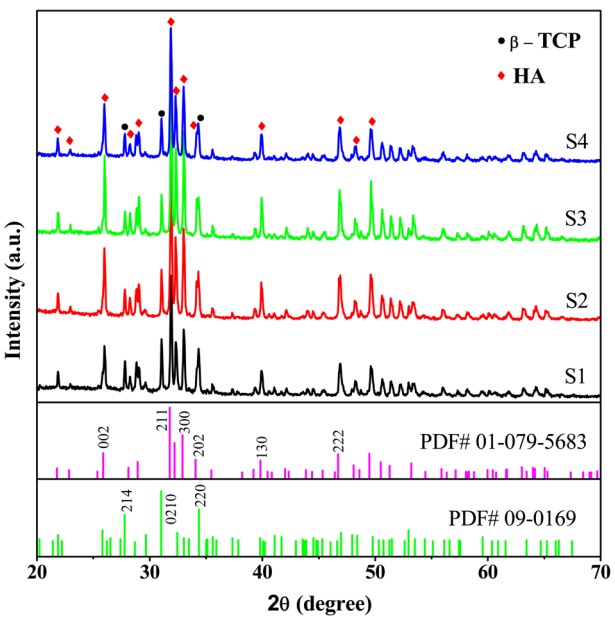

Fig. 2 XRD pattern of all samples S1, S2, S3, and S4.

Table 1 Phases percentage in all composite samples

Sample	S1	S2	S3	S4
HA	89.2	80.2	77.8	71.5
β-TCP	10.8	19.8	22.2	28.5

well, showing the high crystallinity of the hexagonal structure of HA with the *P*63/*m* space group and the secondary phase of orthohombic β-TCP. Consequently, other impurity phases were not observed, indicating that the novel synthesis method produced Er/Yb/Mo-tri doped BCP phosphors with intense dual-mode emission. Moreover, the typical planes corresponding to the HA phase, including those at (002), (211), (112), (300), and (222), as well as those of the β-TCP phase at (214), (0 2 10), and (220), were clearly observed. Among the diffraction peaks, that corresponding to the (211) plane of the HA phase presented the highest intensity, confirming the preferred orientation of crystal growth along this plane (*c* axis). This result is in good agreement with the finding of other works, suggesting the selective enhancement in the bioactivity and biocompatibility of HA.[38,39] Notably, the diffraction peaks of the samples became high and sharply intensified, indicating the high crystallinity degree of the obtained phosphors, leading to the enhanced emission efficiency of the systems due to presence of the cosurfactant PVA. Furthermore, the phase percentage of all samples, as inferred from the XRD data and represented in Table 1, highly depended on PVA content, and the β-TCP phase tended to increase with the increase in PVA content. This phenomenon resulted in a reduction in the content of OH^-, which has a luminescence quenching effect; thus, the emission efficiency of the phosphors improved.[8,28] Howeover, previous works have shown that the degree of crystallinity has a strong effect on the emission efficiency of RE-doped phosphors.[7,40,41] Therefore, the degree of crystallinity of all samples was determined by using eqn (1).[7] The results are shown in Table 2.

$$X_C = 1 - \frac{V_{112/300}}{I_{300}} \quad (1)$$

where I_{300} presents the diffraction peak intensity associated with the (300) plane. $V_{112/300}$ is the intensity of the hollow between (112) and (300) reflections and disappears from non-crystalline samples.[8] Accordingly, the degree of crystallinity of the samples increased (up to 90.93%) with the increase in PVA content, suggesting that the emission efficiency of the phosphors enhanced. This result indicates that the present method is an effective way to improve the crytallinity of the phosphors, thus enhancing emission efficiency.

Furthermore, crystal size was estimated from XRD data by using the Scherrer equation[34] to investigate the effect of the cosurfactant PVA on the crystal size of the phosphors:

$$L = \frac{0.9\lambda}{\beta \cos(\theta)} \quad (2)$$

where L is the crystal size (nm); 0.9 is Scherrer constant; λ is 0.15406 nm associtated with the wavelength of the X-ray sources; and β (radians) and θ (radians) are the full width at half

Table 2 The crystallinity degree of the HA phase and crystal size in all samples

Sample	$2\theta^{o}$	Variable	Intensity	% X_C	L (nm)
S1	33.02	I_{300}	2917	85.02	51.32
	32.32	$V_{112/300}$	437		
S2	33.00	I_{300}	2427	90.93	44.42
	32.32	$V_{112/300}$	220		
S3	33.01	I_{300}	2054	88.60	41.26
	32.33	$V_{112/300}$	234		
S4	33.02	I_{300}	1856	82.50	39.72
	32.32	$V_{112/300}$	325		

maximum and peak position, respectively. In this case, the diffraction peak corresponding to the (211) plane of HA was selected to analyze the broadening of the Bragg line. The L values of all samples with different PVA content are presented in Table 2. The trend wherein the L value decreased with the increase in PVA content indicates that the PVA content (Table 2) can effectively increase the film stiffness obtained from ME systems. Increasing the PVA content enhanced film stiffness, crystallization growth was hindered and crystal size decreased. These results agree well with previous findings[21,32,34,42] and confirm that using a cosurfactant (PVA) could control nuclear growth in crystallization, thereby controlling the crystal size and morphology of the materials.

3.2. FT-IR analysis

Fig. 3 presents the FT-IR spectra of samples S1, S2, and S3 with different cosurfactant PVA contents. These spectra were acquited over 450–4000 cm^{-1}. The HA structure was characterized by typical vibrational modes corresponding to the PO_4^{3-} group, such as 474 (ν_2 mode), 565/603 (ν_4 mode), 963 (ν_1 mode), and 1020/1092 (ν_3 mode) cm^{-1}. The vibrational modes of OH^- groups, including those at 634 (vibration mode) and 3568 (stretching mode) cm^{-1}, indicated the presence of the HA

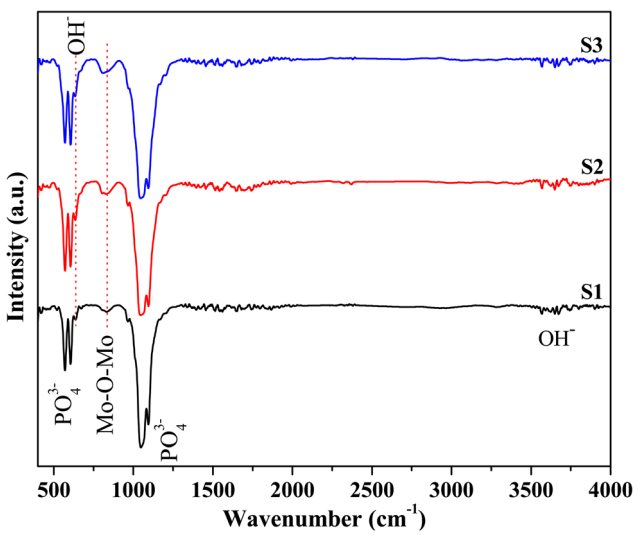

Fig. 3 FT-IR spectra of samples S1, S2, and S3.

structure and H_2O molecules on the surface, respectively. Notably, other peaks attributed to the surfactant and cosurfacetant were absent owing to the high-temperatures heat treatment of the samples. In addition, Mo–O–Mo bindings were characterized by the stretching vibration at 813.6 cm^{-1}, confirming the presence of the Mo^{6+} ion into the host lattice, leading to the formation of the Yb^{3+}–MoO_4^{2-} dimers that improved the UC emission of the phosphors due to energy transfer.[20,43] This result has been clearly observed and explained in detail in our previous works.[7,8,19,20,23]

3.3. Raman shifts spectral analysis

Fig. 4 shows the Raman shift spectra of all the resulting samples. These spectra were acquired over 100–1100 cm^{-1}. In the low-frequency band, the peaks at 115 and 145 cm^{-1} were associated with lattice phonon vibration[44] (Fig. 4a). Meanwhile, the peak at 327 cm^{-1} is related to the symmetrical binding vibration of Ca–OH, which involved OH^- vibrations, and that at 433 cm^{-1} was attributed to the symmetrical bending vibration of ν_2 (symmetric variable-angle vibration) mode of PO_4^{3-}[45] (Fig. 4b). At high frequencies, peaks were observed at 592 and 610 cm^{-1}. These peaks belonged to the ν_4 (antisymmetric variable-angle vibration) mode of PO_4^{3-} groups. The peak with the highest intensity was observed at 964 cm^{-1} and was assigned to the ν_1 (symmetric stretching vibration) of the typical PO_4 unit of phosphate in HA. Moreover, the peaks between 1045 and 1077 cm^{-1} corresponded to the ν_3 (antisymmetric stretching vibration) vibration. Additionally, in good agreement with the FT-IR results, the peaks at 879 cm^{-1} were attributed to the asymmetric stretching of the Mo–O–Mo bonds.[46] Low-intensity peaks ascribed to the β-TCP phase were observed at 949 (ν_1, P–O) and 409 (ν_2, P–O) cm^{-1},[47,48] indicating that the amount of the β-TCP phase that had formed was less than that of the HA phase (Fig. 4c). This finding agreed with the XRD result (Fig. 2 and Table 1).

3.4. XPS analysis

Fig. 5 shows the XPS spectrum measurement of Er-Yb-Mo co-doped HA/β-TCP composite phosphor synthesized by the ME method, ranging from 0 to 1200 eV. The obtained phosphor consists of the host lattice's Ca, P, and O elements and the dopant elements including Er, Yb, Mo. In this case, the Ca element is characterized by the binding energy of Ca 2s, Ca 2p, Ca 3s, and Ca 3p states. The binding energy of Ca 2p is the highest intensity and is used to characterize bonds between the Ca^{2+} ion and the surrounding ligand, and the Ca^{2+} oxidation state. Meanwhile, O and P elements are characterized by the binding energy of O 1s and P 2p states. The dopant elements are determined by the binding energy of the Er 4d, Yb 4d, and Mo 3d states, respectively. Notably, other impurity elements were not observed in this result, indicating the high purity of the prepared phosphors.

Furthermore, the typical binding energy corresponds to the states of the elements in the host lattices, as shown in Fig. 6. Fig. 6a shows the XPS spectrum of Ca 2p that exhibits two binding energies of about 346.89 (Ca $2p_{3/2}$) and 350.35 eV (Ca

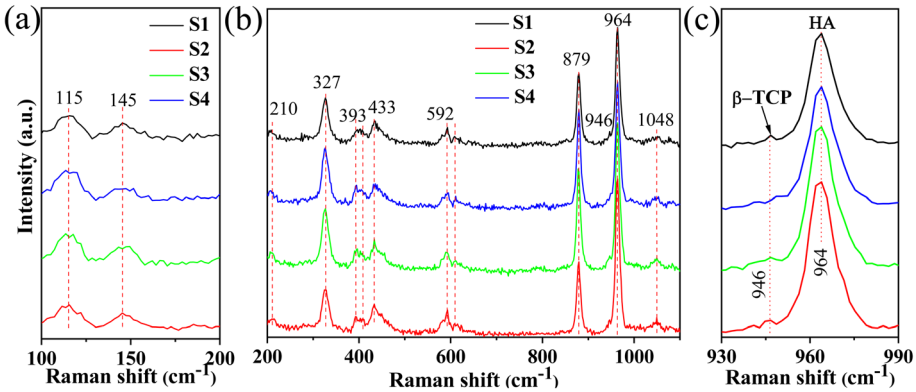

Fig. 4 Raman shifts of samples from 100–200 cm^{-1} (a), 200–1100 cm^{-1} (b), and (c) zoom in from 930 to 990 cm^{-1}.

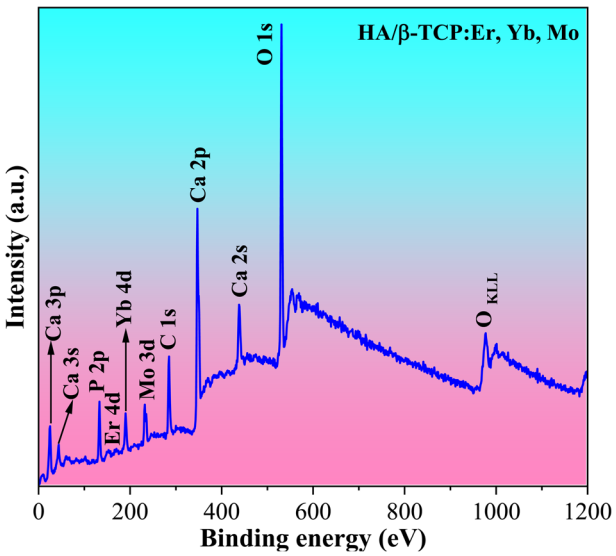

Fig. 5 XPS spectrum of Er-Yb-Mo tri-doped HA/β-TCP composite phosphor.

$2p_{1/2}$), which are characteristic of Ca^{2+} ions in the resulted phosphor.[49] The binding energy at 132.95 eV is associated with the P $2p_{3/2}$ state of P 2p, which indicates the O–P bonds of the HA/β-TCP (Fig. 6b). The binding energy of the O 1 s state (Fig. 6c) includes three peaks centered at 530.90 eV, is attributed to the binding energy of the PO_4^{3-} groups and OH^- group of the HA structure; 532.73 eV corresponds to oxygens of absorbed water on HA/β-TCP surface, and 529.52 eV is characteristic the O–Ca bonds.[49,50] Notably, the Er 4d and Yb 4d signals are centered at 169.50 eV and 190.27 eV, respectively, which is attributed to the binding energy of the Er^{3+} and Yb^{3+} oxidation states in the systems (Fig. 6d and e). The Mo^{6+} oxidation state (Mo 3d) is determined by the binding energy associated with 231.92 eV (Mo $3d_{5/2}$) and 235.07 eV (Mo $3d_{3/2}$), as shown in Fig. 6f.[51] This result agrees with FT-IR (Fig. 3) and Raman shift (Fig. 4) analysis because of the formation of Mo–O–Mo bonds. These results confirm the presence of the elements in the host lattice and the dopant element in the systems. This means obtaining the Yb^{3+}–MoO_4^{2-} dimers and their absorption energy transfer to Er^{3+} ions, forming the intense green UC emission. This result is in good agreement with the phosphor's optical properties (Fig. 8).

3.5. FE-SEM images

Fig. 7 shows the representative FE-SEM surface images of the samples with PVA contents of 5 (7a), 10 (7b), 15 (7c), and 20 ml (7d). The morphologies of all samples exhibited mostly hexagonal and rod-like particles (inset of Fig. 7a), and trace number of spherical particles with a random orientation. The rod-like nanoparticles had a diameter of approximately 100–120 nm and a length of roughly 245–550 nm, whereas hexagonal particles exhibit an average size of about 120–180 nm. The clear grain boundaries of the prepared phosphor confirmed their high crystallinity, which agrees with the XRD result (Fig. 2). The difference in sample morphology was due to the orientation of the hexagonal structure to the measured plane (picture plane). As a result of the presence of the cosurfactant PVA, numerous tube-like structures with orientations (hexagon with *c* axis) to the *c* axis parallel to the measured plane were observed. In this case, the presence of nanorod-like morphology in the systems at high temperature treatment (1000 °C) suggested that the cosurfactant PVA in the ME method supports the thermal stability of the nanorod-like phosphor particles, instead of spherical particles.[7,8,20,24,33,34] These results could influence the optical properties of the systems. Previous works[23,52] have indicated that the formation of the rod-like structures could reduce the total internal reflections due to the enriched waveguide effect of the nanorods and help increase transmittance. This effect in turn results in an enhancement in light output that is synonymous with a consequent improvement in UC emission intensity, leading to the increased emission efficiency of phosphors.

3.6. Optical properties

Fig. 8a shows the PL UC emission of samples with different PVA cosurfactant contents annealed at 1100 °C for 2 h in air. Notably all samples presented intense green UC emission at 520/550 nm that corresponded to $^2H_{11/2}/^4S_{3/2}$–$^4I_{15/2}$ transitions but weak red UC emission at 656 nm attributed to the $^4F_{9/2}$–$^4I_{15/2}$ transition,

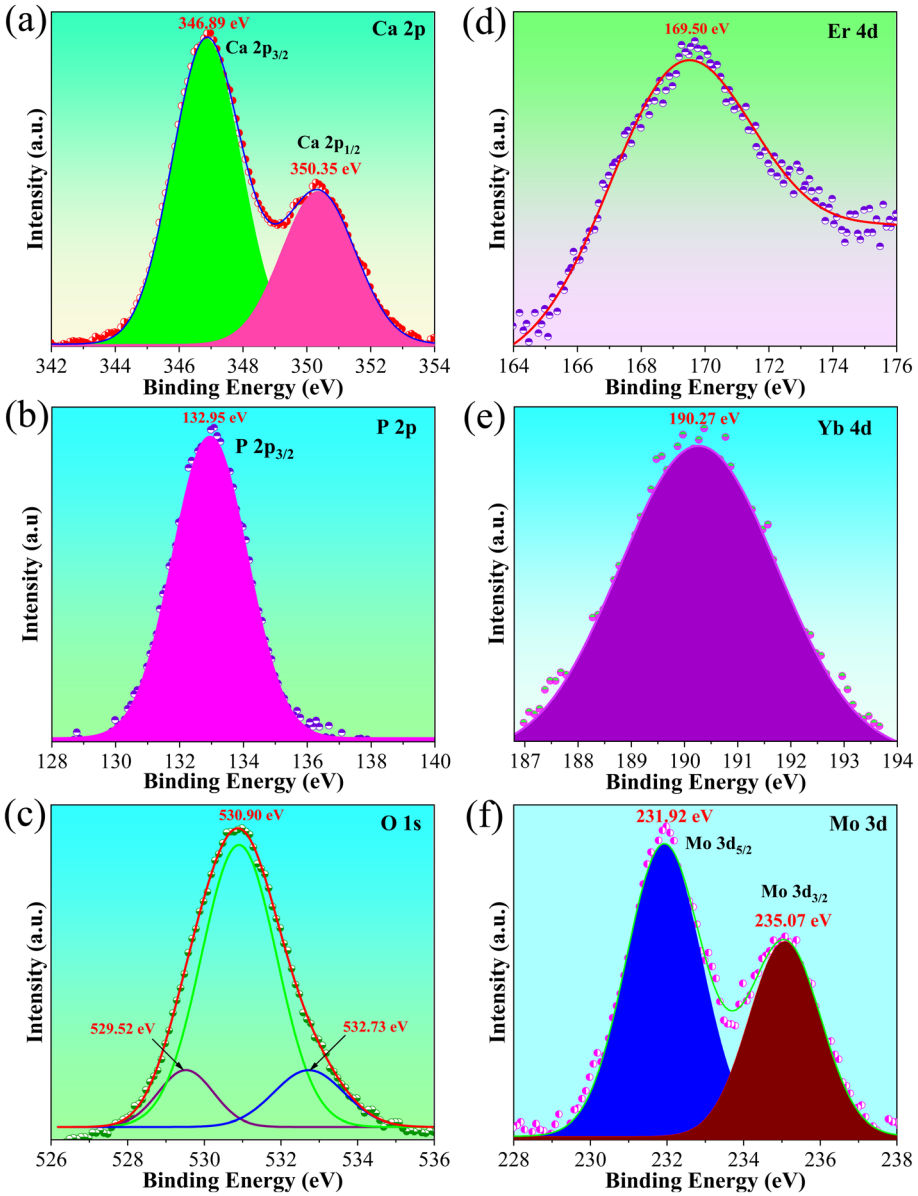

Fig. 6 XPS spectrum of typical elements in the phosphor, (a) Ca 2p spectrum, (b) P 2p spectrum, (c) O 1s spectrum, (d) Er 4d spectrum, (e) Yb 4d spectrum, and (f) Mo 3d spectrum.

suggesting the dominance of green emission in the systems. The selective enhancement in green UC emission was due to energy transfer from the $|^2F_{7/2}$, $^3T_2>$ level of the $Yb^{3+}-MoO_4^{2-}$ dimer to the $^4F_{7/2}$ level of the Er^{3+} ion in Er/Yb/Mo tri-doped system that has been well explained in previous works.[8,23,53,54] The phenomenon was confirmed by the XPS results of forming Mo^{6+} and Yb^{3+} oxidation states in the systems, leading to forming $Yb^{3+}-MoO_4^{2-}$ dimers. Notably, the emission intensity of the samples depended on PVA content and reached its maximum value when 10 ml PVA was used as a cosurfactant (Fig. 8b). In this case, the presence of the cosurfactant PVA in the system resulted in the formation of rod-like nanoparticles and a high degree of crystallinity, which causes emission efficiency to enhance remarkably. Montalbano *et al.*[55] observed that HA nanorods can be combined with collagen to prepare collagen/nano-HA hybrid systems as a material for 3D printing scaffolding. Meanwhile, K. Lin[56] confirmed that using HA nanorods as raw materials is an effective way to obtain dense bioceramics with high mechanical properties. Therefore, the preferred orientation of the rod-like particles of the acquired phosphors makes them suitable for biomedical applications. The green/red intensity ratios shown in Fig. 8c tended to increase with increasing PVA content, indicating that the PVA cosurfactant supported the selective enhancement in green emission. Additionally, the color coordinates of samples were estimated to confirm the dominance of green emission. The result for S2 sample was close to those for pure green light-based phosphors (0.231, 0.692), making it suitable for solid-state lighting applications (Fig. 8d).

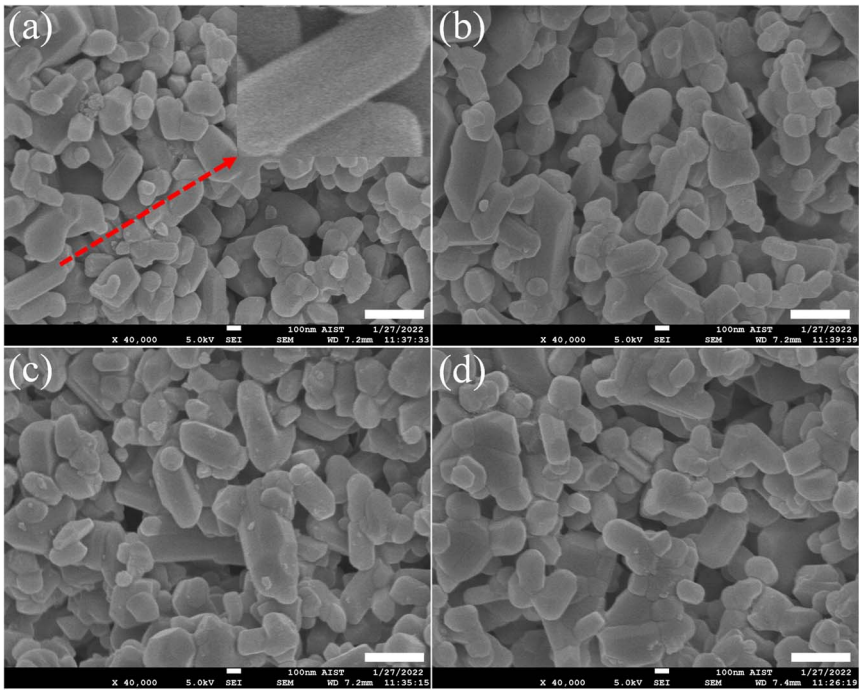

Fig. 7 SEM images of all samples, (a) S1, (b) S2, (c) S3, and (d) S4, scale bar 400 nm.

Furthermore, the color purity of the samples was calculated by using Commission International de l'Eclairage (CIE) coordinates.[57]

$$\text{Color purity} = \frac{\sqrt{(x-x_i)^2+(y-y_i)^2}}{\sqrt{(x_d-x_i)^2+(y_d-y_i)^2}} \times 100\% \quad (3)$$

where (x, y) are the color coordinates of the obtained samples; $(x_i = 0.3333, y_i = 0.3333)$ is the color coordinate of the white light source; and (x_d, y_d) indicate the color coordinates of the dominant wavelength.[11] These values were introduced into eqn (3). The color purity of samples investigated is shown in Table 3. The investigated phosphors clearly showed high color purity, which reached 94.77% for the S2 sample. These results confirm that the phosphors could be suitable for solid-state lighting applications. Furthermore, S2, which had the highest intensity among samples, was chosen to explore thermal sensing characteristics, as discussed in the next section.

3.6.1 UC emission mechanisms. The dependence of emission intensity on the power excitation of lasers from 200 mW to 600 mW is shown in Fig. 9 to evaluate the UC mechanism. Emission intensity corresponds to both green and red regions increase when power excitation increases (Fig. 9a). Notably, the dependence of emission intensity (I) on power excitation (P) can be described by the equation $I \propto P^n$, where n is the number of photons absorbed to produce green and red UC emission in phosphors.[18] The resulting fitting of the above equation indicates that the value of n for green emission was 2.02 and 1.83 for green emissions and was 1.63 for red emissions, suggesting two-photon absorption processes to produce UC emissions. The n value for green emission was considerably higher than that for red emission, indicating that green emission increased faster than red emission as the pump power increased. Furthermore, the number of photons absorbed could be used to propose the energy level diagram of RE ion-doped phosphors to evaluate their emission behaviors, as was done in our previous studied and other works.[8,18,53,58]

3.7. Optical temperature sensing properties

Fig. 10a represents the temperature-dependent PL intensity of the S2 sample at 293–533 K under 975 nm excitation. Upon $^2H_{11/2}$–$^4I_{15/2}$ transition, its emission intensity slightly increased when the temperature increased. On the other hand, the $^4S_{3/2}$ – $^4I_{15/2}$ transition was sensitive to temperature, and its value significantly decreased with an increase in temperature. This effect can be further clearly observed in Fig. 10c. Notably, the emission intensity at 413 K was 63% compared with that at 293 K, indicating the excellent stability of the sample. Moreover, the phosphor showed high-intensity emission at high temperatures (533 K), demonstrating its temperature stability and applicability at high temperatures. The change in emission intensity at typical temperatures (293, 373, and 533 K) are shown in Fig. 10b. The emission intensity changes in two levels $^2H_{11/2}$ (I_{528})/$^4S_{3/2}$ (I_{550}) and level $^4F_{9/2}$ (I_{658}), due to temperature, as shown in Fig. 10c. Furthermore, the relationship between the I_{528}/I_{550} ratio and the ΔE (energy gap between the two-levels) are used to estimate the optical temperature sensor characteristics, can be written as:[59]

$$\text{FIR} = \frac{I_{525}}{I_{546}} = Ae^{-\frac{\Delta E}{kT}} \quad (4)$$

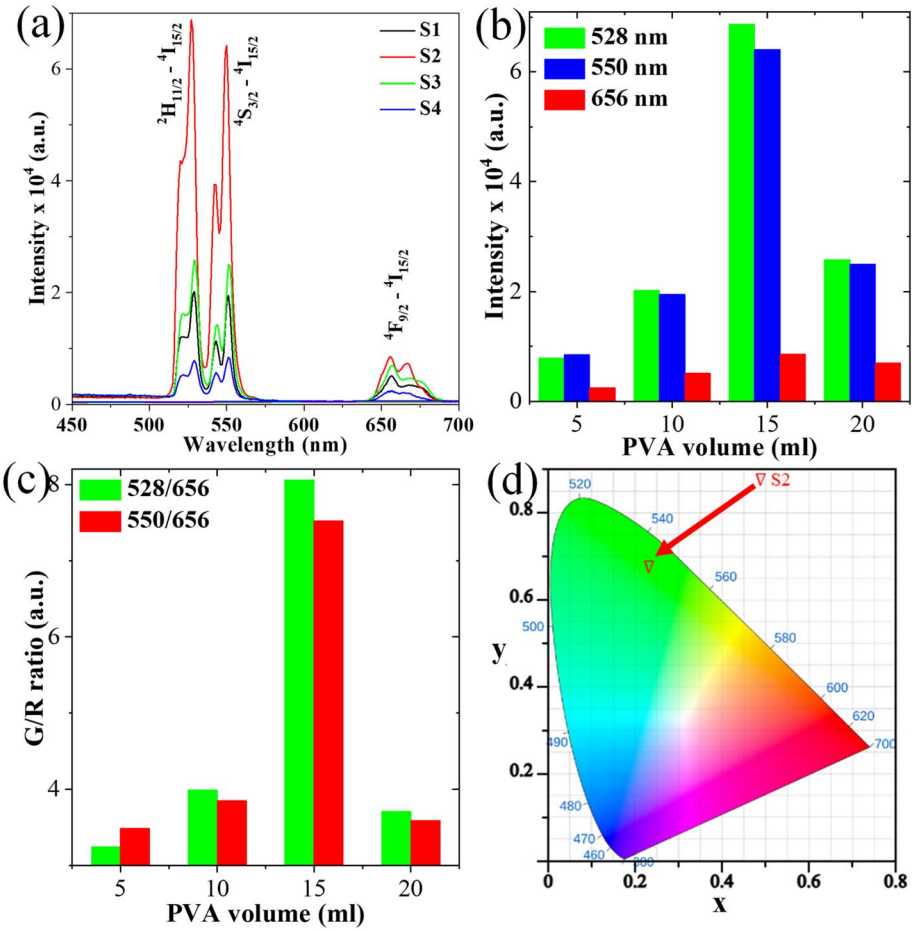

Fig. 8 (a) UC emission spectrum of samples S1, S2, S3, and S4; (b) emission intensity as a function of PVA content; (c) green/red intensity ratio of all samples; and (d) color purity of all resulting samples.

Table 3 CIE chromaticity coordinates and color purity of samples

Samples	Chromaticity coordinates (x, y)	Color purity (%)
S1	(0.246, 0.562)	62.20
S2	(0.231, 0.692)	94.77
S3	(0.248, 0.559)	68.50
S4	(0.250, 0.422)	61.36

where A presents a pre-exponential constant, $k = 0.6950348\ \mathrm{cm}^{-1}\ \mathrm{K}^{-1}$ is the Boltzmann constant, and the T is absolute temperature. The natural logarithm of eqn (4) was taken to obtain eqn (5):

$$\mathrm{Ln(FIR)} = -\frac{\Delta E}{k}\frac{1}{T} + \ln A \quad (5)$$

A simple linear equation based on eqn (5) was used for fitting to estimate ΔE and A parameters, as shown in Fig. 10d.

The value of relative sensitivity is a key parameter that is needed to evaluate thermal sensing performance and can be written as:[60]

$$S = \frac{1}{\mathrm{FIR}}\frac{d}{\mathrm{d}T}(\mathrm{FIR}) = \frac{\Delta E}{kT^2} \quad (6)$$

Fig. 10e indicates that the maximum value of relative sensitivity was 0.93% K^{-1} at 293 K. Recent works have reported that RE-doped UC phosphors[8,61–63] with sensitivities ranging from 0.0033 K^{-1} to 0.0093 K^{-1} could be used for optical temperature sensors. These results indicate that phosphors based on HA/β-TCP: Er/Yb/Mo fabricated *via* the ME method could be used for thermal sensing applications. Furthermore, the sensitivity of the phosphor in this work and other studies were compared to checking the fabricated phosphor's performance (Table 4). As shown in Table 4, the phosphor obtained in this work presented higher value compared with other host lattices such as phosphate,[68] tungstate,[67] and aluminate,[60] while showed lower value compared with other host lattice, including vanadate,[63] fluoride,[64] TZLB,[66] and oxide.[5] Furthermore, it showed high temperature sensitivity (0.93% K^{-1}) based on the operating temperature range (293–533 K) that is prospective for thermal sensing applications.

The difference between the temperature calculated by using the FIR technique and actual experimental temperature read

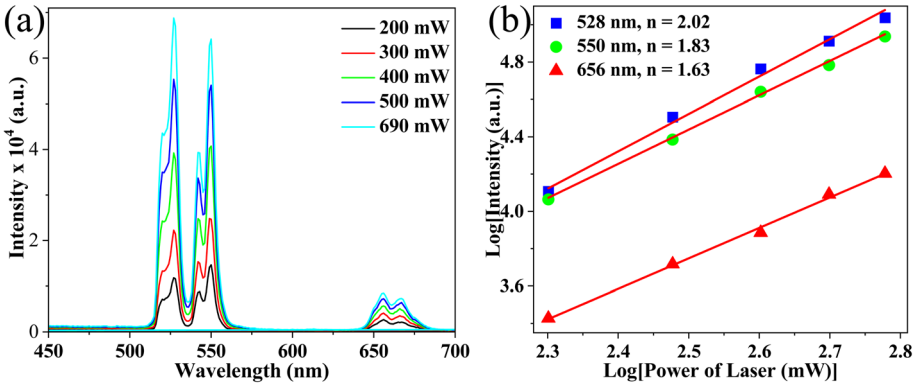

Fig. 9 Emission intensity-dependent power excitation of sample S2.

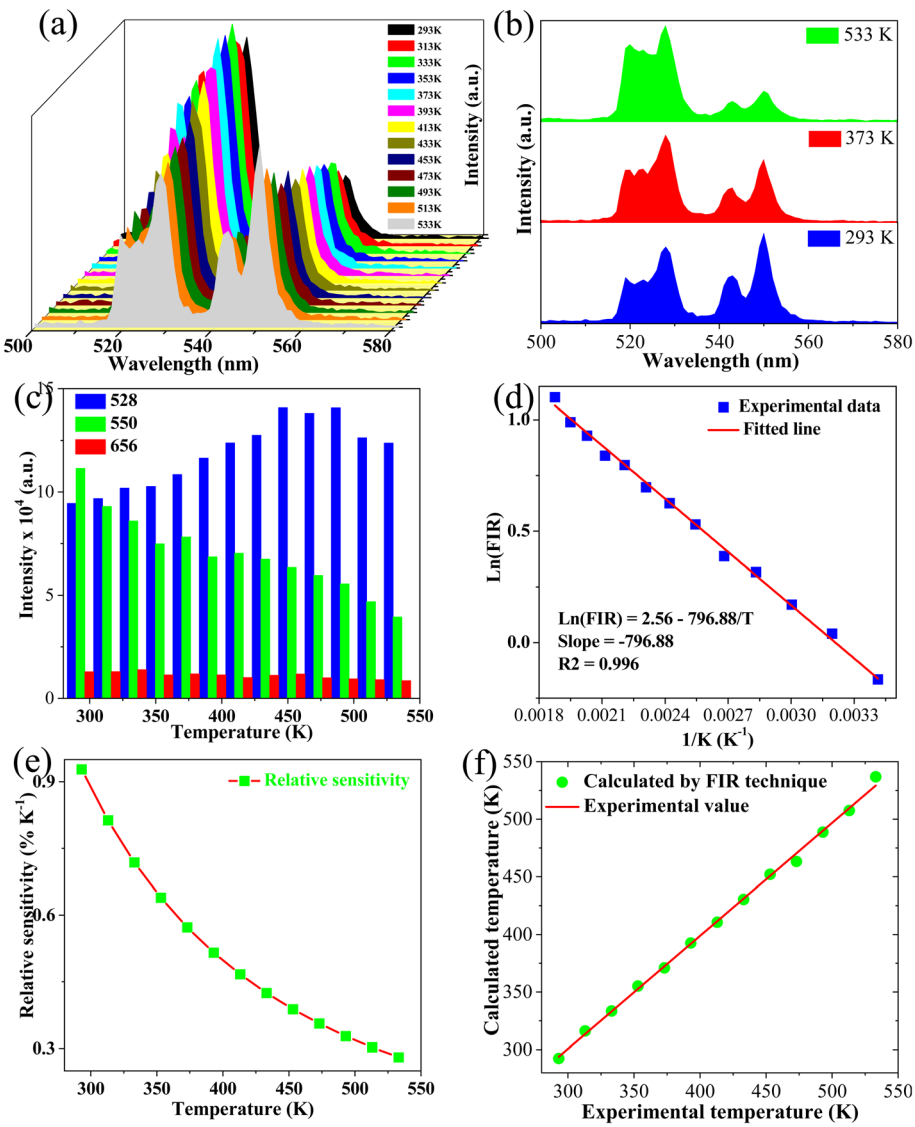

Fig. 10 (a) Green emission spectra of S2 sample with different temperatures ranging from 293 K to 533 K, (b) comparison of green UC emissions of the S3 sample at some selected temperatures (2933, 363, and 533 K), (c) green and red emission intensity as a function of temperature, (d) monolog of the FIR as a function of inverse absolute temperature, (e) sensor sensitivity as a function of the temperature, and (f) the relationship between calculated temperature and actual experimental temperature.

Table 4 Comparision of sensitivity sensor of UC phosphor in this work with other UC phosphors

Materials	ΔE	Maximum sensitivity (K^{-1})	Temperature range (K)	References
$Na_2YMg_2(VO_4)_3$	699.00	0.0104	303–573	64
Sr_2GdF_7: Er/Yb	1048.00	0.0167	300–660	65
TZLB: Er, Yb, Mo	452.00	0.0124	298–420	66
Gd_2O_3: Er/Yb	1059.00	0.0151	298–558	5
Ca_2MgWO_6: Er/Yb	698.00	0.0092	303–573	67
$ZnAl_2O_4$: Er, Yb	561.82	0.0070	298–473	60
$Sr_{10}(PO_4)_6O$: Er/Yb	925.60	0.005951	303–723	68
HA/β-TCP: Er/Yb/Mo	553.83	0.0093	293–533	This work

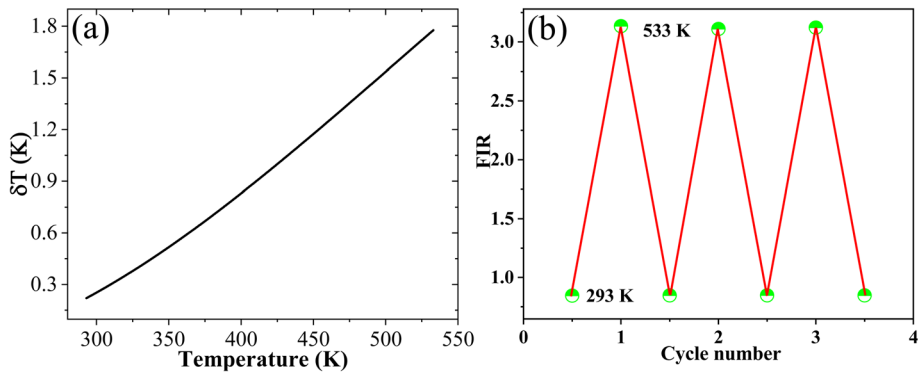

Fig. 11 (a) Corresponding temperature resolution of sample S2, and (b) corresponding cycling measurements.

directly from the thermo couple was used to confirm the reliability of the measurement and determined by using eqn (6):[8]

$$T = \frac{\Delta E}{k} \frac{1}{\ln A - \ln(FIR)} \quad (7)$$

Fig. 10f reveals that a small difference existed between the two values, as confirmed by the high correlation coefficient $R^2 = 0.999$, indicating the reliability and accuracy of the FIR technique.

Furthermore, the critical parameters such as temperature resolution (δT) and repeatability (R) were calculated to confirm the phosphor's suitability for thermal sensor applications, using the following equations:[19]

$$\delta T = \frac{1}{S_r} \times \frac{\delta \mathrm{FIR}}{\mathrm{FIR}} \quad (8)$$

$$R = 1 - \frac{\max(\Delta_m - \Delta_i)}{\Delta_m} \quad (9)$$

where δFIR presents the standard deviation of the FIR value. Δ_m is the value of FIR at 293 and 533 K. Δ_i means the FIR value in three consecutive irradiation cycles. Resulting calculations indicate that the minimum value of δT was 0.22 K at 293 K, as shown in Fig. 11a. Meanwhile, Fig. 11b confirmed an excellent thermal repeatability (R > 99%) of the FIR values in three consecutive cycles. These results indicate that HA/β-TCP: Er/Yb/Mo composite phosphors are a promising material for optical-thermometer applications.

4. Conclusion

A novel ME method for the synthesis of HA/β-TCP: Er/Yb/Mo composite phosphors with intense green UC emission and good thermal sensing properties using PVA as a cosurfactant was investigated. The obtained phosphors containing PVA exhibited a mixture of phases (HA and β-TCP) with a high crystallinity. Under 975 nm wavelength excitation, the phosphors showed intense green UC emission at 528/550 nm and weak red emission at 656 nm, and their intensity depended on PVA content. Furthermore, the phosphors possessed high color purity (up to 94.77%) and good thermal sensitivity (0.93% K^{-1} at 293 K), suggesting it is suitable for solid lighting and thermal sensing applications. This finding indicates that the prepared phosphors are a promising material for thermal sensing and optoelectronic devices. Overall, controlling the content of the cosurfactant PVA to modulate structure and morphology is an attractive approach to acquire excellent UC emission and thermal sensing properties that promote extended applications.

Data availability

The data supporting this article have been included as part of the article.

Author contributions

Do Danh Bich: data curation, format analysis, investigation. Nguyen Viet Tung: format analysis, investigation. Vuong-Hung

Pham: project administration, format analysis. Duy-Hung Nguyen: data curation, resources. Cao Xuan Thang: funding acquisition, conceptualization, investigation, format analysis, writing – review & editing. Hoang Nhu Van: conceptualization, format analysis, methodology, resources, supervision, project administration, writing – original draft, writing – review & editing.

Conflicts of interest

The authors declare that they have no known competing financial interests or personal relationships that could have appeared to influence the work reported in this paper.

Acknowledgements

Funding: This research was funded by the Ministry of Education and Training under grant number B2025-BKA-03.

References

1 Y. Wang, L. Lei, R. Ye, G. Jia, Y. Hua, D. Deng and S. Xu, Integrating Positive and Negative Thermal Quenching Effect for Ultrasensitive Ratiometric Temperature Sensing and Anti-counterfeiting, *ACS Appl. Mater. Interfaces*, 2021, **13**, 23951–23959.

2 Y. Zhao, X. Wang, Y. Zhang, Y. Li and X. Yao, Optical temperature sensing of up-conversion luminescent materials: Fundamentals and progress, *J. Alloys Compd.*, 2020, **817**, 152691.

3 W. Zheng, B. Sun, Y. Li, R. Wang, T. Lei and Y. Xu, Near-Infrared Laser-Triggered Full-Color Tuning Photon Upconversion and Intense White Emission in Single Gd_2O_3 Microparticle, *ACS Sustain. Chem. Eng.*, 2020, **8**, 2557–2567.

4 K. Li, D. Li, M. Jia, D. Guo, M. Dai, J. Zhao, G. Chen and Z. Fu, Li-Based Nanoprobes with Boosted Photoluminescence for Temperature Visualization in NIR Imaging-Guided Drug Release, *Nano Lett.*, 2025, **25**, 776–785.

5 R. S. Baltieri, A. Reupert, D. Manzani and L. Wondraczek, Remote Luminescent Temperature Sensing Using 3D-Printed Eu(III)-Doped Micropolymers at the Tip of an Optical Fiber, *Adv. Mater. Technol.*, 2025, **10**, 2401877.

6 B. Cao, Y. Bao, Y. Liu, J. Shang, Z. Zhang, Y. He, Z. Feng and B. Dong, Wide-range and highly-sensitive optical thermometers based on the temperature-dependent energy transfer from Er to Nd in Er/Yb/Nd codoped $NaYF_4$ upconversion nanocrystals, *Chem. Eng. J.*, 2020, **385**, 123906.

7 H. Nhu Van, L. T. Cuong, D. H. Nguyen, L. T. Tam and V. H. Pham, Effect of Sr substituted on multifunction pure green emission of rare-earth-element doped HA/β-TCP nanocomposite for optical thermometer, *Ceram. Int.*, 2024, 1–10, DOI: **10.1016/j.ceramint.2024.07.119**.

8 D. D. T. Thuy, V. T. N. Minh, T. N. Xuan, P. Van Huan, V. P. Hung, D. H. Nguyen, B. T. Hoan, T. Le Manh and H. N. Van, Dual-mode green emission and temperature sensing properties of rare-earth-element-doped biphasic calcium phosphate composites, *J. Alloys Compd.*, 2021, **871**, 159483.

9 W. Ran, G. Sun, X. Ma, Z. Zhang and T. Yan, Excellent upconversion luminescence and temperature sensing performance of $CdMoO_4$: Er^{3+},Yb^{3+} phosphors, *Dalton Trans.*, 2022, **51**, 8749–8756.

10 J. Zhu, T. Yang, H. Li, Y. Xiang, R. Song, H. Zhang and B. Wang, Improving the up/down-conversion luminescence *via* cationic substitution and dual-functional temperature sensing properties of Er^{3+} doped double perovskites, *Chem. Eng. J.*, 2023, **471**, 144550.

11 M. Wang, S. Ding, C. Zhang, H. Ren, Y. Zou, X. Tang and Q. Zhang, Pure-green upconversion emission and high-sensitivity optical thermometry of Er^{3+}-doped stoichiometric $NaYb(MoO_4)_2$, *Ceram. Int.*, 2023, **49**, 37661–37669.

12 L. Liu, H. Liu, W. Zou and S. Ding, Er^{3+} doping $YbTaO_4$ phosphors: upconversion luminescence and temperature sensing characteristics, *Ceram. Int.*, 2023, **49**, 28500–28505.

13 D. Song, W. Liu, Z. Yin, X. Li, Q. Wang, X. Yan, X. Zhang, F. Wang, Y. Qin, Y. Shen, Z. Zhang, Y. Zhao and T. Cheng, A temperature sensor based on Er^{3+}/Yb^{3+} co-doped tellurite fiber for real-time thermal monitoring of transformers, *Ceram. Int.*, 2023, **49**, 28878–28885.

14 X. Wang, P. Zhang, X. Wang, R. Lei, L. Huang, S. Xu and S. Zhao, Fluorescent sensing probe based on heterovalent doped $Lu_2W_{2.5}Mo_{0.5}O_{12}$: Er^{3+}/Yb^{3+} phosphor for real-time chip temperature monitoring, *Ceram. Int.*, 2023, **49**, 34560–34568.

15 X. Wang, Q. Liu, Y. Bu, C. S. Liu, T. Liu and X. Yan, Optical temperature sensing of rare-earth ion doped phosphors, *RSC Adv.*, 2015, **5**, 86219–86236.

16 A. Banwal and R. Bokolia, Enhanced upconversion luminescence and optical temperature sensing performance in Er^{3+} doped $BaBi_2Nb_2O_9$ ferroelectric ceramic, *Ceram. Int.*, 2022, **48**, 2230–2240.

17 J. Xing, F. Shang and G. Chen, Upconversion luminescence of Yb^{3+}/Er^{3+} co-doped $NaSrPO_4$ glass ceramic for optical thermometry, *Ceram. Int.*, 2021, **47**, 8330–8337.

18 H. T. Nam, P. D. Tam, N. Van Hai and H. N. Van, Multifunctional optical thermometry using dual-mode green emission of $CaZrO_3$: Er/Yb/Mo perovskite phosphors, *RSC Adv.*, 2023, **13**, 14660–14674.

19 C. V. Thai, N. T. Dung, N. V. Hai, V. T. N. Minh, N. X. Truong, P. A. Tuan, P. V. Huan and H. N. Van, Intense green upconversion emission of rare-earth-doped $Sr_3(PO_4)_2$/$Sr_2P_2O_7$ powder: effect of annealing temperature and temperature-sensor properties, *Optik*, 2022, **264**, 169446.

20 H. N. Van, V. N. Hung, P. H. Vuong, P. V. Huan, B. T. Hoan, N. D. Hung and L. M. Tu, A novel upconversion emission material based on Er^{3+}–Yb^{3+}–Mo^{6+} tridoped Hydroxyapatite/Tricalcium phosphate (HA/β-TCP), *J. Alloys Compd.*, 2020, **827**, 154288.

21 Z. Zeng, H. Feng, M. Hao and Y. Zhang, One-pot approach to form *in situ* colchicine-containing nano-hydroxyapatite within microemulsion composite system for sustained transdermal delivery, *Compos. Commun.*, 2021, **25**, 100698.

22 L. O. Ahmed and R. A. Omer, Hydroxyapatite biomaterials: a comprehensive review of their properties, structures, clinical applications, and producing techniques, *Rev. Inorg. Chem.*, 2024, **6**, 1–26.
23 H. N. Van, L. M. Tu, D. T. T. Dung, P. H. Vuong, N. D. Hung, P. T. H. Diep and H. V. Hung, On enhancement and control of green emission of rare earth co-doped hydroxyapatite nanoparticles: synthesis and upconversion luminescence properties, *New J. Chem.*, 2021, **45**, 751–760.
24 H. N. Van, P. D. Tam, V. H. Pham, D. H. Nguyen, C. X. Thang and L. Quoc Minh, Control of red upconversion emission in Er^{3+}–Yb^{3+}–Fe^{3+} tri-doped biphasic calcium phosphate, *Inorg. Chem. Commun.*, 2023, **150**, 110538.
25 S. Basu and B. Basu, Unravelling Doped Biphasic Calcium Phosphate: Synthesis to Application, *ACS Appl. Bio Mater.*, 2019, **2**, 5263–5297.
26 M. Šupová, Substituted hydroxyapatites for biomedical applications: a review, *Ceram. Int.*, 2015, **41**, 9203–9231.
27 U. Sabu, G. Logesh, M. Rashad, A. Joy and M. Balasubramanian, Microwave assisted synthesis of biomorphic hydroxyapatite, *Ceram. Int.*, 2019, **45**, 6718–6722.
28 H. N. Van, P. D. Tam, N. D. T. Kien, P. T. Huy and V. H. Pham, Enhancing the luminescence of Eu^{3+}/Eu^{2+} ion-doped hydroxyapatite by fluoridation and thermal annealing, *Luminescence*, 2017, **32**, 817–823.
29 Y. Sun, H. Yang and D. Tao, Microemulsion process synthesis of lanthanide-doped hydroxyapatite nanoparticles under hydrothermal treatment, *Ceram. Int.*, 2011, **37**, 2917–2920.
30 I. D. Rojas-Montoya, P. Fosado-Esquivel, L. V. Henao-Holguín, S. Ramírez-Rave, M. J. Bernad-Bernad and J. Gracia-Mora, Hydroxyapatite nanoparticles synthesized *via* reverse microemulsions and their adsorption/desorption properties with enrofloxacin, *J. Cryst. Growth*, 2020, **549**, 125878.
31 C. García, C. García and C. Paucar, Controlling morphology of hydroxyapatite nanoparticles through hydrothermal microemulsion chemical synthesis, *Inorg. Chem. Commun.*, 2012, **20**, 90–92.
32 X. Ma, Y. Chen, J. Qian, Y. Yuan and C. Liu, Controllable synthesis of spherical hydroxyapatite nanoparticles using inverse microemulsion method, *Mater. Chem. Phys.*, 2016, **183**, 220–229.
33 A. Huang, H. Dai, X. Wu, Z. Zhao and Y. Wu, Synthesis and characterization of mesoporous hydroxyapatite powder by microemulsion technique, *J. Mater. Res. Technol.*, 2019, **8**, 3158–3166.
34 V. C. Arun Prakash, I. Venda, V. Thamizharasi and E. Sathya, A new attempt on synthesis of spherical nano hydroxyapatite powders prepared by dimethyl sulfoxide - poly vinyl alcohol assisted microemulsion method, *Mater. Chem. Phys.*, 2021, **259**, 124097.
35 E. Vafa, R. Bazargan-Lari and M. E. Bahrololoom, Electrophoretic deposition of polyvinyl alcohol/natural chitosan/bioactive glass composite coatings on 316L stainless steel for biomedical application, *Prog. Org. Coatings.*, 2021, **151**, 106059.
36 Y. Li, L. Li, Y. Ma, K. Zhang, G. Li, B. Lu, C. Lu, C. Chen, L. Wang, H. Wang and X. Cui, 3D-Printed Titanium Cage with PVA-Vancomycin Coating Prevents Surgical Site Infections (SSIs), *Macromol. Biosci.*, 2020, **20**, 1–8.
37 R. Hussain, S. Tabassum, M. A. Gilani, E. Ahmed, A. Shaif, F. Manzoor, A. T. Shah, A. Asif, F. Sharif, F. Iqbal and S. A. Siddiqi, *In situ* synthesis of mesoporous polyvinyl alcohol/hydroxyapatite composites for better biomedical coating adhesion, *Appl. Surf. Sci.*, 2016, **364**, 117–123.
38 W. Shi, Z. Liu, I. Yamada, D. Noda, T. Kataoka, K. Shinozaki and M. Tagaya, Effective Thermal Diffusion of Eu(III) and F Ions into Hydroxyapatite Nanoparticles by Citric Acid Coordinative Mediation, *ACS Appl. Nano Mater.*, 2023, **6**, 2346–2355.
39 M. Gu, W. Li, L. Jiang and X. Li, Recent progress of rare earth doped hydroxyapatite nanoparticles: luminescence properties, synthesis and biomedical applications, *Acta Biomater.*, 2022, **148**, 22–43.
40 H. Jin, H. Wu and L. Tian, Improved luminescence of Y_2MoO_6: Eu^{3+} by doping Li^+ ions for light-emitting diode applications, *J. Lumin.*, 2012, **132**, 1188–1191.
41 B. Han, B. Liu, Y. Dai, J. Zhang and H. Shi, Alkali metal ion substitution induced luminescence enhancement of $NaLaMgWO_6$: Eu^{3+} red phosphor for white light-emitting diodes, *Ceram. Int.*, 2019, **45**, 3419–3424.
42 V. Collins Arun Prakash, I. Venda, V. Thamizharasi and E. Sathya, A comparative study on microemulsion synthesis of hydroxyapatite powders by ionic and Non-Ionic surfactants, *Mater. Today Proc.*, 2021, **51**, 1701–1705.
43 A. Shandilya and K. Sreenivas, Upconversion luminescence studies in (Er^{3+}, Yb^{3+}, and Mo^{6+}) tri-doped $SrWO_4$ ceramics, *J. Lumin.*, 2023, **253**, 119438.
44 G. Cheng, Y. Zhang, H. Yin, Y. Ruan, Y. Sun and K. Lin, Effects of strontium substitution on the structural distortion of hydroxyapatite by rietveld refinement and Raman Spectroscopy, *Ceram. Int.*, 2019, **45**, 11073–11078.
45 K. Prem Ananth, B. Guo, C. Zhang, W. Wang, P. Zhou and J. Bai, Investigation of biphasic calcium phosphate (BCp)/polyvinylpyrrolidone (PVp)/graphene oxide (GO) composite for biomedical implants, *Ceram. Int.*, 2020, **46**, 24413–24423.
46 A. K. Cuentas-Gallegos, C. Frausto, L. A. Ortiz-Frade and G. Orozco, Raman spectra of hybrid materials based on carbon nanotubes and Cs 3PMo12O40, *Vib. Spectrosc.*, 2011, **57**, 49–54.
47 C. S. Ciobanu, S. L. Iconaru, F. Massuyeau, L. V. Constantin, A. Costescu and D. Predoi, Synthesis, Structure, and Luminescent Properties of Europium-Doped Hydroxyapatite Nanocrystalline Powders, *J. Nanomater.*, 2012, **2012**, 942801.
48 M. Wang, X. Ge, Z. Cui, S. Wu, S. Zhu, Y. Liang, Z. Li and W. W. Lu, Influences of strontium on the phase composition and lattice structure of biphasic calcium phosphate, *Ceram. Int.*, 2021, **47**, 16248–16255.

49 G. Ciobanu, A. M. Bargan and C. Luca, New cerium(IV)-substituted hydroxyapatite nanoparticles: Preparation and characterization, *Ceram. Inter.*, 2015, **41**, 12192–12201.
50 H. N. Van, Effect of Al^{3+} content on optical properties and Judd–Ofelt intensity parameters in novel red emission HA/β-TCP: Eu, Al composite phosphor, *Ceram. Inter.*, 2025, DOI: 10.1016/j.ceramint.2025.03.395.
51 H. N. Tran, S. Park, F. T. A. Wibowo, N. V. Krishna, J. H. Kang, J. H. Seo, H. N. Phu, S. Y. Jang and S. Cho, *Adv. Sci.*, 2020, 2002395.
52 J. H. Oh, L. K. Bharat, J. H. Jeong, Y. S. Huh and J. S. Yu, $(BaSr)_2SiO_4$: Eu^{2+} nanorods with enhanced luminescence properties as green-emitting phosphors for white LED applications, *Dyes Pigm.*, 2017, **142**, 447–456.
53 Y. Cong, D. Liu, N. Yu, Y. Xiao, Q. Yang and Y. Fu, Strong green upconversion emission from Er^{3+}–Yb^{3+}–Mo^{6+} tridoped ZrO_2, *Mater. Chem. Phys.*, 2014, **144**, 440–443.
54 Y. Cong, B. Dong, N. Yu, Y. He, Y. Zhao and Y. Yang, Enhanced upconversion emission in ZrO_2–Al_2O_3 composite oxide, *Dalton Trans.*, 2016, **45**, 6627–6633.
55 G. Montalbano, G. Molino, S. Fiorilli and C. Vitale-Brovarone, Synthesis and incorporation of rod-like nano-hydroxyapatite into type I collagen matrix: a hybrid formulation for 3D printing of bone scaffolds, *J. Eur. Ceram. Soc.*, 2020, **40**, 3689–3697.
56 K. Lin, J. Chang, R. Cheng and M. Ruan, Hydrothermal microemulsion synthesis of stoichiometric single crystal hydroxyapatite nanorods with mono-dispersion and narrow-size distribution, *Mater. Lett.*, 2007, **61**, 1683–1687.
57 N. V. Hai, D. T. Hien, N. T. K. Linh, B. T. Hoan, N. M. Tu and H. N. Van, Blue-excited red emission of CeO_2:Eu^{3+}, Al^{3+} cubic phosphor: influence of Al^{3+} ion doping and Judd-Ofelt theory, *J. Lumin.*, 2023, **263**, 120047.
58 X. Yang, Z. Fu, Y. Yang, C. Zhang, Z. Wu and T. Sheng, Optical Temperature Sensing Behavior of High-Efficiency Upconversion: Er^{3+}–Yb^{3+} Co-Doped $NaY(MoO_4)_2$ Phosphor, *J. Am. Ceram. Soc.*, 2015, **98**, 2595–2600.
59 H. Liu, M. Dai, K. Li, H. Xu, Y. Wei and Z. Fu, Paradigm Enhancement of White-Light Responsive NIR-II Photoluminescence *via* Toroidal Energy Migration, *Adv. Opt. Mater.*, 2025, **13**, 2402398.
60 H. Liang, Z. Luo, W. Lei, P. Zhang, S. Liu, Z. Zhou and A. Lu, Preparation, crystallization kinetics, and optical temperature sensing properties of Er^{3+}–Yb^{3+} co-doped fluorosilicate glass-ceramics containing $ZnAl_2O_4$ crystals, *J. Alloys Compd.*, 2022, **895**, 162673.
61 X. Chai, J. Li, X. Wang, H. Zhao, Y. Li and X. Yao, Dual-mode photoluminescence, temperature sensing and enhanced ferroelectric properties in Er-doped $(Ba_{0.4}Ca_{0.6})TiO_3$ multifunctional diphase ceramics, *Mater. Sci. Eng. B*, 2015, **201**, 23–28.
62 S. Sinha and K. Kumar, Studies on up/down-conversion emission of Yb^{3+} sensitized Er^{3+} doped $MLa_2(MoO_4)_4$ (M = Ba, Sr and Ca) phosphors for thermometry and optical heating, *Opt. Mater.*, 2018, **75**, 770–780.
63 A. K. Singh, S. K. Singh, B. K. Gupta, R. Prakash and S. B. Rai, Probing a highly efficient dual mode: down-upconversion luminescence and temperature sensing performance of rare-earth oxide phosphors, *Dalton Trans.*, 2013, **42**, 1065–1072.
64 Y. Tong, W. N. Zhang, R. F. Wei, L. P. Chen and H. Guo, $Na_2YMg_2(VO_4)_3$:Er^{3+},Yb^{3+} phosphors: up-conversion and optical thermometry, *Ceram. Int.*, 2021, **47**, 2600–2606.
65 Y. Pan, X. Wei, W. Wang, H. Chen and Y. Li, Monodispersed Sr_2GdF_7:Yb^{3+}, Er^{3+} nanocrystals: hydrothermal synthesis and optical temperature sensing behavior, *Opt. Mater.*, 2020, **107**, 110156.
66 Z. Yin, W. Liu, D. Song, X. Chen, Q. Wang, X. Zhou, F. Wang, X. Yan, X. Zhang, T. Suzuki, Y. Ohishi and T. Cheng, Luminescence enhanced temperature sensor based on the up-conversion emission in Er^{3+}/Yb^{3+}/Mo^{6+} tri-doped tellurite fiber, *Ceram. Int.*, 2023, **49**, 18906–18911.
67 Y. C. Jiang, Y. Tong, S. Chen, W. Zhang, F. Hu, R. Wei and H. Gao, A three-mode self-referenced optical thermometry based on up-conversion luminescence of Ca_2MgWO_6: Er^{3+},Yb^{3+} phosphors, *Chem. Eng. J.*, 2021, **413**, 127470.
68 S. Cui and G. Chen, Enhanced up-conversion luminescence and optical thermometry characteristics of Er^{3+}/Yb^{3+} co-doped $Sr_{10}(PO_4)_6O$ transparent glass-ceramics, *J. Am. Ceram. Soc.*, 2020, **103**, 6932–6940.